A combined time-of-flight and depth-of-interaction detector for total-body positron emission tomography

Eric Berg[a] and Emilie Roncali
Department of Biomedical Engineering, University of California, Davis, One Shields Avenue, Davis, California 95616

Maciej Kapusta
Molecular Imaging, Siemens Healthcare, Knoxville, Tennessee 37932

Junwei Du and Simon R. Cherry
Department of Biomedical Engineering, University of California, Davis, One Shields Avenue, Davis, California 95616

(Received 28 September 2015; revised 7 January 2016; accepted for publication 10 January 2016; published 26 January 2016)

Purpose: In support of a project to build a total-body PET scanner with an axial field-of-view of 2 m, the authors are developing simple, cost-effective block detectors with combined time-of-flight (TOF) and depth-of-interaction (DOI) capabilities.
Methods: This work focuses on investigating the potential of phosphor-coated crystals with conventional PMT-based block detector readout to provide DOI information while preserving timing resolution. The authors explored a variety of phosphor-coating configurations with single crystals and crystal arrays. Several pulse shape discrimination techniques were investigated, including decay time, delayed charge integration (DCI), and average signal shapes.
Results: Pulse shape discrimination based on DCI provided the lowest DOI positioning error: 2 mm DOI positioning error was obtained with single phosphor-coated crystals while 3–3.5 mm DOI error was measured with the block detector module. Minimal timing resolution degradation was observed with single phosphor-coated crystals compared to uncoated crystals, and a timing resolution of 442 ps was obtained with phosphor-coated crystals in the block detector compared to 404 ps without phosphor coating. Flood maps showed a slight degradation in crystal resolvability with phosphor-coated crystals; however, all crystals could be resolved. Energy resolution was degraded by 3%–7% with phosphor-coated crystals compared to uncoated crystals.
Conclusions: These results demonstrate the feasibility of obtaining TOF–DOI capabilities with simple block detector readout using phosphor-coated crystals. [http://dx.doi.org/10.1118/1.4940355]

Key words: positron emission tomography (PET), time-of-flight (TOF), depth-of-interaction (DOI), scintillator, phosphor coating

1. INTRODUCTION

We are aiming to construct a high sensitivity, total-body clinical PET scanner by extending the axial field-of-view (FOV) to maximize geometric detection efficiency and approach the fundamental sensitivity limits of PET (explorer.ucdavis.edu). The proposed scanner (EXPLORER) consists of 36 rings (79.5 cm ring diameter), each with 48 detector modules, providing an axial FOV of 196 cm. Monte Carlo simulations showed that a long axial FOV PET scanner could achieve 40-fold higher peak noise equivalent count ratio (NECR) compared to current state-of-the-art clinical PET scanners with a 20 cm axial field-of-view,[1,2] which will allow whole-body images to be acquired for the first time with roughly 40-fold higher statistics, or at 1/40th dose, or in 1/40th the time compared to current procedures.

The expected substantial sensitivity gains and total-body imaging capabilities may open new areas of study with PET: (1) Whole-body tissue kinetic modeling studies to image the distribution of new compounds within all organs simultaneously,[3] (2) simultaneous acquisition of brain and body data to study multisystem processes involved in psychiatry, metabolism, and inflammatory conditions,[4] (3) longitudinal studies to track tumor response to treatment, and (4) studying neurodevelopmental disorders such as autism and schizophrenia in the pediatric population. High sensitivity PET will also allow imaging radiotracers over a greater number of half-lives. This will enable, for example, enhanced tumor detection sensitivity with FDG and ultrastaging of micrometastatic disease.[5]

With a long axial field-of-view PET scanner, a large acceptance angle (maximum ring difference) should be allowed for pairs of annihilation photons to maximize geometric detection efficiency.[1] However, axial detector penetration of obliquely incident gammas detected within this wide acceptance angle will introduce significant depth-of-interaction (DOI) parallax error, leading to degraded spatial resolution that may offset sensitivity gains. One possible alternative to minimize DOI parallax error is to reduce the thickness of scintillator arrays, but detection efficiency and NECR gain are then greatly reduced.[1] Thick detectors with DOI capability should

therefore be used. With using crystal sizes commonly used in clinical scanners (~4×4×20 mm^3), we expect 2- or 3-bin DOI encoding (~6 mm DOI resolution) to be sufficient to reduce parallax errors in oblique lines-of-response to an acceptable level.

Incorporating time-of-flight (TOF) reconstruction improves image SNR,[6] due to suppression of image noise from nontrue coincidence events. In a long axial field-of-view PET scanner, excellent timing precision (<500 ps) will help suppress random coincidences and allow a variable coincidence window dependent on the length of the line-of-response. Along with this, given the larger effective object size (due to the longer path length of gammas traveling obliquely through the patient), TOF should provide an increased gain in effective sensitivity.[7]

A recent Monte Carlo simulation study of a 2 m axial length PET scanner showed that combining 2-bin DOI encoding with 400 ps timing resolution increased the SNR by 44% relative to 600 ps timing resolution and no DOI encoding,[8] demonstrating the need for detectors with TOF–DOI capabilities for a long axial field-of-view PET scanner.

Due to the large number of detectors in the EXPLORER scanner, we require a cost-effective and simple TOF–DOI encoding method compatible with traditional detector readout (high degree of multiplexing) and manufacturing processes. A suitable detector module design is the conventional PET block detector,[9] where a large crystal array is coupled via a light guide to four photomultiplier tubes (PMTs). The block detector is still used in most state-of-the-art clinical PET scanners due to its simple architecture, component reliability, minimal heat load, and relatively low-cost. Conversely, the detector simplicity limits the possible DOI encoding techniques.[10] The well-established phoswich method has previously been implemented in a PET block detector.[11] However, the optical mismatch between the scintillator layers results in poor transmission of scintillation light through the interface, leading to degraded timing resolution.

We have proposed a method to combine TOF–DOI capabilities using single ended photodetector readout by applying a phosphor coating on scintillator crystals to induce depth-dependent changes in the signal shape (Fig. 1). For a given scintillation event, a fraction of the light is absorbed and converted by the phosphor and re-emitted after a delay according to the phosphor's intrinsic decay time. Using an appropriate pulse shape discrimination technique, DOI information can be extracted from the digitized pulses.[12] This method was first developed for a DOI encoding detector for preclinical PET (Ref. 1) and was recently investigated for TOF–DOI feasibility.[14,15] In TOF-DOI studies, a 3×3×10 mm polished lutetium oxyorthosilicate (LSO) crystal coated with phosphor provided DOI information with negligible impact on the signal rise time, and a timing resolution <400 ps.

Here we extend phosphor-coating studies to a clinical PET block detector. First, using single phosphor-coated scintillator crystals directly coupled to a PMT, we investigated the impact of the phosphor-coating geometry on detector performance. Single crystal studies provided convenient means to develop and optimize signal processing methods to be used in block detector studies and provided baseline detector performance under ideal conditions. A clinical block detector was modified to include a different phosphor coating configuration in each quadrant of the scintillator array. We investigated the TOF–DOI abilities of the block detector as well as the impact of phosphor coating on energy resolution and crystal resolvability in flood maps.

2. MATERIALS AND METHODS

2.A. Scintillator crystals and detector modules

The PET block detector module was fabricated by Siemens (Siemens Medical Solutions, Knoxville, TN) and is similar to detectors used in the Siemens mCT scanner,[16] but optimized toward enhanced timing resolution. The detector contains a 12×12 array of LSO (Ref. 17) crystals coupled to four PMTs (R9800, Hamamatsu Corp.) via a 6 mm thick light guide. The crystal array size is 48.0 × 48.0 mm^2 and each crystal is 3.94×3.94×20 mm^3 with chemically etched surfaces. Specular reflector (ESR, 3M) is used to optically isolate the

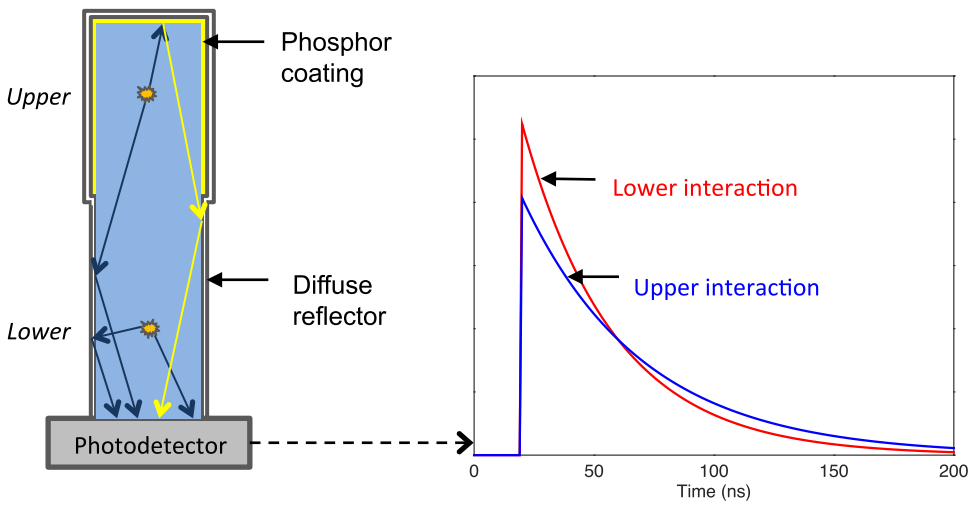

FIG. 1. The phosphor coating absorbs a fraction of the scintillation photons depending on the interaction depth. Delayed photon emission from the phosphor results in depth-dependent signal shape changes.

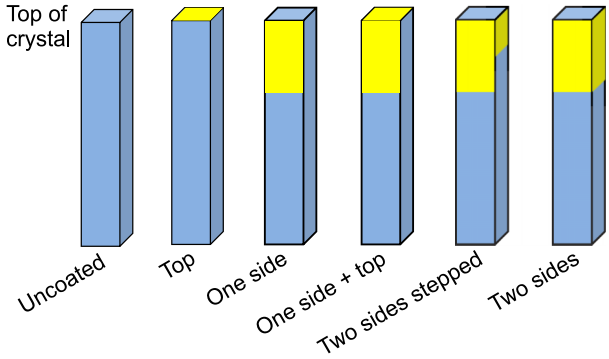

FIG. 2. Illustration of phosphor coating configurations considered in this study. Shaded areas near the top of the crystal denote phosphor coating.

crystals on their lateral sides while a Teflon sheet covers the top surface of the crystal array. The crystals are coupled to the light guide using a pressure sensitive adhesive. The detector module contains five outputs: four PMT anode signals are readout via Ethernet connection and the signals from the last dynode are summed and readout via a microcoaxial connector. The entire module is housed in a thin mu-metal casing. One of the corner crystals was removed from the adhesive and was wrapped in Teflon for the single crystal experiments. The same crystal was used for all single crystal experiments.

2.B. Coating the crystals

Crystals were coated using a compound containing 65% (by weight) cerium-doped yttrium aluminium garnet (YAG:Ce, $Y_3(Al)_5O_{12}$:Ce, Comtech International, Inc., Korea) phosphor powder and 35% optical cement (NOA 88, Norland Products, NJ) as described by Roncali *et al.*[18] A thin coating layer (100 μm thickness) was manually applied to the desired crystal surface before being cured for ~200 s with a UV lamp (Super Spot MK II, Lesco UV, CA). The decay time of the phosphor was measured to be 58 ns. The peak excitation wavelength of YAG:Ce at 430 nm closely matches the LSO emission peak, while the peak emission of YAG:Ce is at 530 nm.

Five coating configurations were considered for this work along with an uncoated crystal (Fig. 2) based on our previous studies with phosphor-coated crystals.[19] The coating length along the lateral sides was 7 mm except for the 3 mm length short coating with the two sides stepped configuration. For the block detector, crystals were manually removed from the block assembly prior to applying the phosphor coating and no visible damage to the light guide adhesive was observed. All phosphor-coating configurations except the one side + top configuration were compared in the scintillator array by applying a different coating to each of the four 6×6 crystal quadrants (Fig. 3).

2.C. Experimental setup

2.C.1. Single crystals

Crystals were wrapped with three layers of Teflon tape and coupled to the center of a R9800 PMT using optical grease (BC-630, Bicron). The crystals were tested with both head-on and side-on (fixed depth) irradiation with 511 keV photons (Fig. 4). All measurements with single crystals were performed in coincidence with a reference detector consisting of a polished $3\times3\times10$ mm^3 LSO crystal coupled to a R9800 PMT. For side-on irradiation, the reference detector was oriented perpendicular to the long side of the phosphor-coated crystal and the reference detector was translated laterally to vary the irradiation position as shown in Fig. 4.[20] The electronically collimated beam width at the phosphor-coated crystal was estimated to be 2–3 mm. All PMTs were biased at −1400 V. Detector signals were digitized at 5 GS/s using a DRS-based digitizer and each digitized pulse spanned 200 ns. Head-on measurements were repeated three times for each crystal with the crystal recoupled to the PMT face between each measurement. Using a 320 kBq ^{68}Ge point source, 25×10^3 events were acquired for each head-on measurement. Using a 530 kBq ^{22}Na point source with a diameter of 0.25 mm, 10×10^3 events were acquired at each of five irradiation positions (2, 6, 10, 14, and 18 mm from the PMT face) with side-on irradiation.

2.C.2. Block detector

The experimental setup for the block detector was nearly identical to that used for the single crystal experiments. All five outputs from the block detector module (4 PMT anode

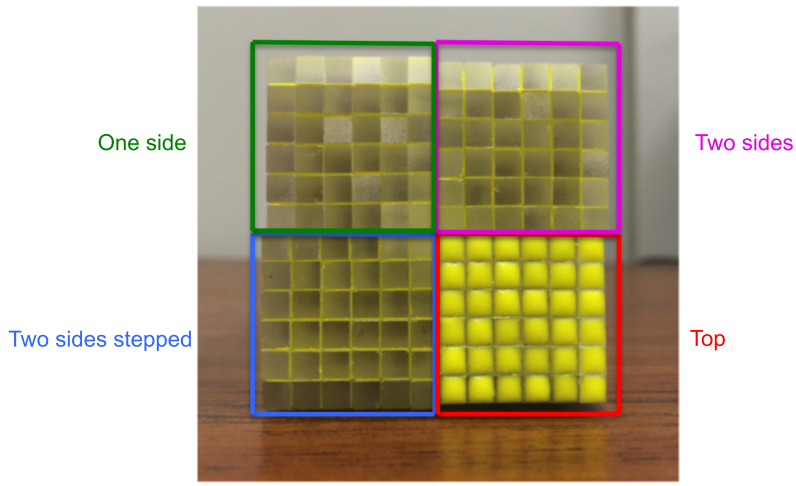

FIG. 3. Phosphor-coated quadrants used in the block detector. Array size is not uniform due to increased crystal pitch caused by phosphor coating.

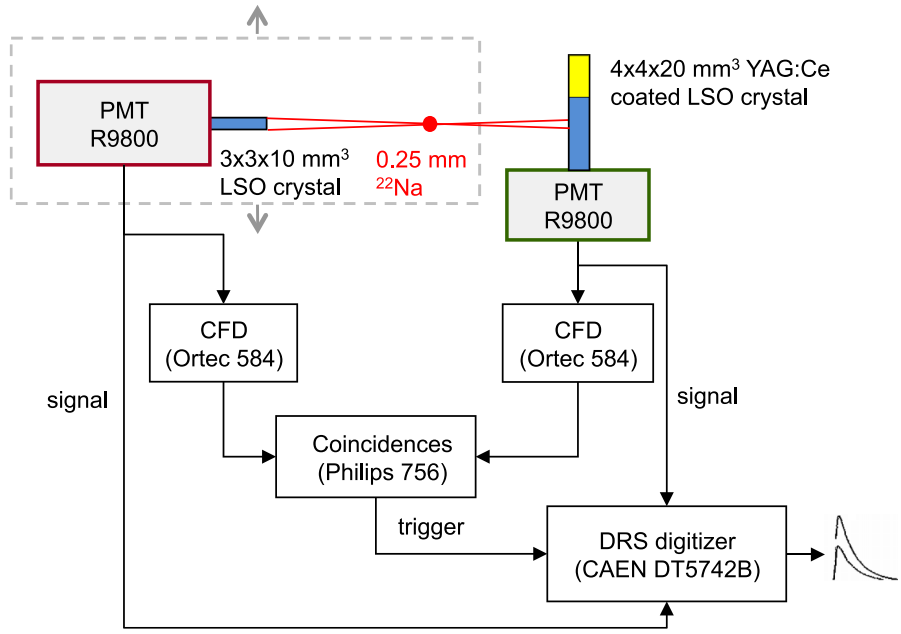

FIG. 4. Experimental setup for testing single-coated crystals in side-on configuration. For head-on measurements, the coated crystals were rotated 90° to face the $3\times3\times10$ mm^3 reference crystal.

+ 1 dynode sum) were amplified using fixed gain, high bandwidth amplifiers (TI4302, Texas Instruments, Dallas, TX). The four anode signals were split into two arms with one arm directly digitized while the second arm was summed and used for coincidence discrimination with the reference detector. The amplified dynode sum signal was directly digitized. The block detector was also tested with head-on and side-on irradiations. For head-on measurements, the distance between the reference detector and block detector module was increased to ~60 cm to allow uniform irradiation of the scintillator array (the ^{68}Ge source was placed near the reference detector) and the same reference detector was used as described for the single crystal experiments. For side-on measurements, a $2\times2\times20$ mm^3 LYSO crystal was used in the reference detector with one of the 2×20 mm^2 faces coupled to the PMT to allow a fan-like irradiation beam. Side-on measurements were acquired separately for each quadrant given the limited irradiation width of the collimated fan-beam with the ^{22}Na point source. For each head-on irradiation to generate flood maps, 10×10^6 events were recorded, while for timing and energy analysis, 2×10^6 events were recorded. For side-on measurements to assess DOI encoding capabilities, 200×10^3 events were recorded at each irradiation depth for each quadrant. Head-on and side-on measurements were first performed with the unmodified detector module prior to applying the phosphor coatings. The same measurements were repeated with the detector module following crystal coating.

2.D. Signal processing and analysis

The light signal collected by the PMT was estimated by integrating the digitized signal over 150 ns after the timing pick-off. The integral values were histogrammed into energy spectra and the photopeak was fitted with a Gaussian distribution. The position of the 511 keV photopeak was used as the light collection metric. Energy resolution was computed as the ratio between the FWHM and mean of the Gaussian fit. For all further analysis in this paper, an energy window of 420–750 keV was applied to the recorded events. For the block detector modules, the dynode sum signal was used for energy analysis.

Digital leading edge (LE) and constant fraction discrimination (CFD) were used to compute timing pick-offs. For the block detector, timing pick-offs were obtained using both the software sum of the four anode signals and the dynode sum signal. The leading edge threshold was optimized for each coating configuration in both single crystal and block detector measurements. A CFD delay of 1.2 ns was used for all configurations. The timing pick-off of the reference detector was obtained using LE discrimination. Time stamps for each event were computed as the time difference between the timing pick-offs of the test detector and the reference detector. Timing spectra were generated by histogramming the time stamps and the FWHM of a Gaussian fit to the timing spectra was used to compute timing resolution. The intrinsic timing resolution of the reference detector (220 ps) was subtracted in quadrature from the measured timing resolution and the estimated coincidence timing resolution for two identical test detectors is reported for all results presented in this paper.

$$\mathrm{DCI}=\frac{\int_{W_1}s(t)dt}{\int_{W_2}s(t)dt}. \quad (1)$$

Three pulse shape discrimination methods were compared: decay time, delayed charge integration (DCI) (Fig. 5) and average signal shapes. Decay time was estimated for each digitized signal using a linear fit to the logarithm of the falling edge of the digitized signal. DCI values were computed as

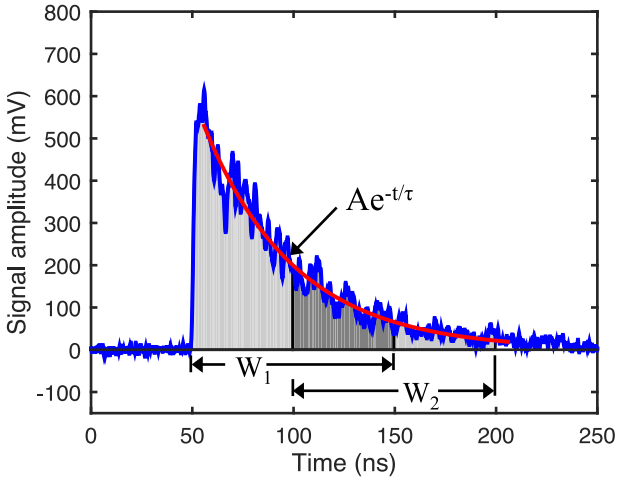

FIG. 5. Decay time and DCI pulse shape discrimination.

the ratio of signal integrals over two time windows [Eq. (1)]. The integration width and delay used for DCI pulse shape discrimination were optimized according to Du *et al.*[13] and an integration width of 105 ns and a delay of 65 ns were used. These values were used for all coating configurations.

For average signal shape analysis, each raw signal was digitized and preprocessed as follows. The signal was normalized according to its integrated energy value and time-aligned with time zero corresponding to one of the leading edge timing pick-offs. Linear interpolation was used to determine signal trace values between the measured digitized values with time sampling of 200 ps. The time-aligned and normalized signals were stored for DOI analysis. For pulse shape discrimination for the block detector experiments, the dynode sum signal was used.

For measurements with the block detector, the scintillation light centroid coordinates of each event were computed using conventional Anger logic,[21] using the four anode signal integrals. The computed coordinates of all events were histogrammed using a 256×256 image array to create flood maps used to identify the crystals. Flood maps were segmented to generate crystal look-up-tables for energy, DOI, and timing analysis.

2.E. DOI classification and positioning error

A DOI classification algorithm was developed similar to that described by Roncali *et al.*[12] Using side-on data for each crystal, 2000 signals were stored from each irradiation depth. Using each pulse shape discrimination method, 1000 of these were classified (test dataset) and 1000 were used to train the classifier (training dataset). The mean decay time and DCI values were computed for the 1000 training signals at each irradiation depth and stored in the classifier as the reference values. The average signal shape at each irradiation position was computed by averaging the 1000 time-aligned and energy normalized raw signal shapes in the training data sets.

The DOI classification process for each test event was as follows: For decay time and DCI metrics, the test event was assigned to the DOI bin corresponding to the reference decay time/DCI value that most closely matched that of the test event. For average signal shapes, the test event was assigned to the DOI bin corresponding to the average signal shape that minimized the RMS difference between the test event and the average signal shapes.

DOI encoding was assessed by computing the DOI positioning error. Since the true DOI of each test event is known from the side-on irradiation position, the DOI error for each event is the absolute distance between the true and estimated DOI. The reported DOI positioning error is the mean DOI error using all test events.

3. RESULTS

3.A. Single crystals

3.A.1. DOI encoding

Histograms of the measured decay time and DCI values as well as the variation of average signal shapes at each irradiation depth demonstrate depth-dependent signal shape changes (Fig. 6). Data are shown for the two sides stepped coating configuration. DCI pulse shape discrimination provided larger separation between distribution peak positions with depth compared to decay time. The width of the distributions was also reduced with DCI pulse shape discrimination, with less

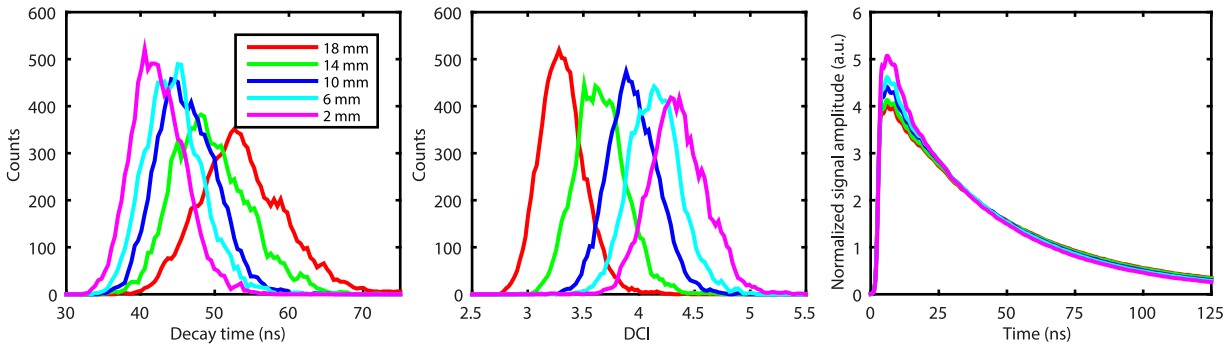

FIG. 6. Histograms of (a) decay time, (b) DCI values, and (c) the average signal shape obtained with each side-on irradiation position for the two sides stepped coating configuration.

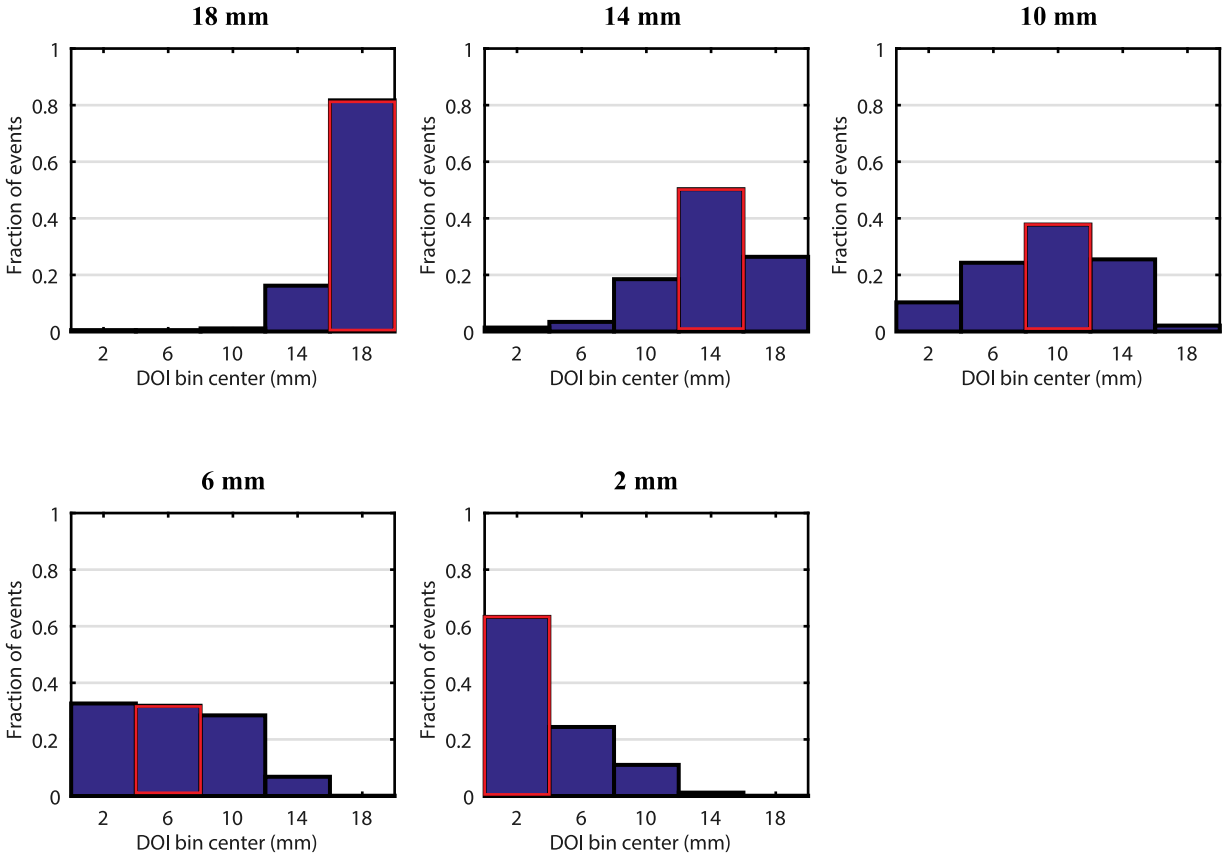

FIG. 7. Classification distributions using DCI pulse shape discrimination with the two sides stepped coating configuration. The 18 mm irradiation position (i.e., 2 mm from top of the crystal) displayed the highest classification sensitivity: at this depth, 81% of the events were correctly classified for the data shown. The correct DOI bin for each plot is indicated by the red outline.

overlap of the distributions and greater uniformity of distribution widths.

Classification distributions (fraction of test events placed in each DOI bin) for all irradiation positions are given in Fig. 7 using the two sides stepped coating configuration and DCI pulse shape discrimination. In general for all coating configurations, the 18 mm irradiation position (top of the crystal) showed the highest fraction of correctly classified events.

The DOI positioning error for each irradiation depth is shown in Fig. 8(a) for DCI pulse shape discrimination. Consistent with classification results, the 18 mm DOI bin typically shows the lowest positioning error. The DOI positioning

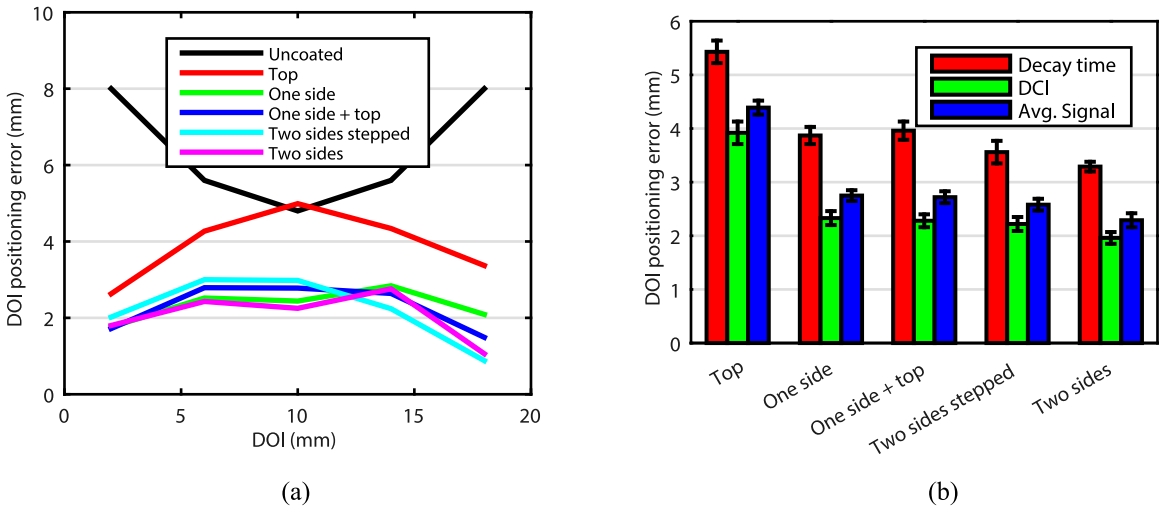

FIG. 8. (a) DOI positioning error computed at each side-on irradiation position using DCI pulse shape discrimination. All coating configurations generally showed lowest DOI positioning error at the 18 or 2 mm irradiation positions. (b) Average DOI positioning error for all coating configurations and pulse shape discrimination methods. DCI discrimination provides superior DOI encoding for all coating configurations, <2 mm with two sides coated.

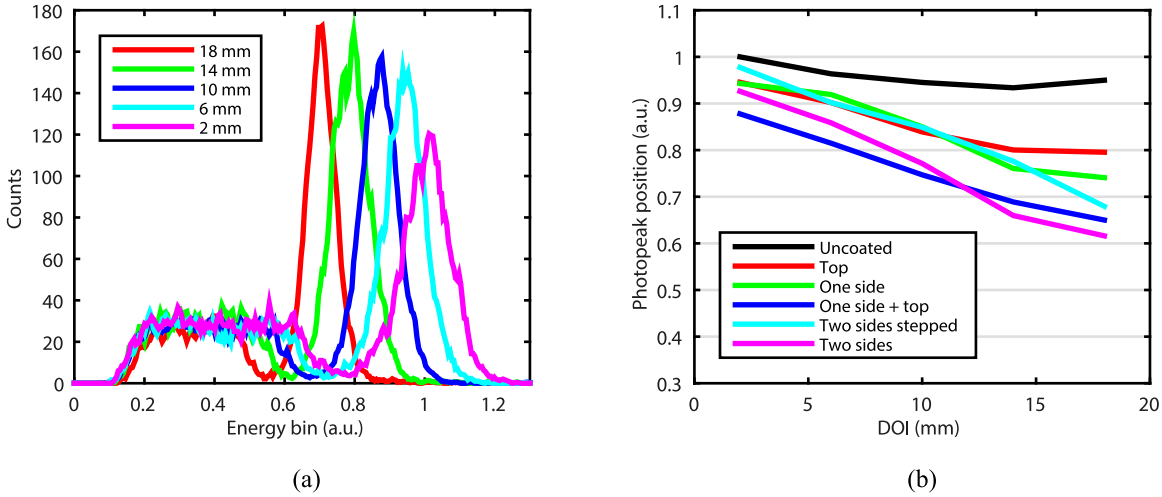

FIG. 9. (a) Energy spectra obtained at each side-on irradiation position with the two sides stepped coating configuration. (b) Changes in photopeak position vs DOI for all coating configurations. The photopeak positions are normalized according the photopeak position of the uncoated crystal at 2 mm.

error of the uncoated crystal is shown for comparison and is computed by assuming no correlation of DOI metrics with depth and therefore randomly assigning the test events to DOI bins. The mean DOI positioning error over all depths was computed for each coating configuration and pulse shape discrimination method [Fig. 8(b)]. Error bars were computed by separating the side-on events into three datasets and computing the average standard deviation of the DOI error across all DOIs. DCI pulse shape discrimination provided the best DOI performance for all coating configurations, as low as 1.9 mm with the two sides coated configuration. With this classification method, the mean DOI positioning error for an uncoated crystal is 6.4 mm, and therefore with DCI pulse shape discrimination, all crystals except top coated show a factor of ~3 improvement in DOI positioning error compared to the uncoated crystal.

We also investigated estimating DOI as a weighted average of the three individual DOI estimates (decay time, DCI, and average signal shape). We found the optimal weighting factors to be 0.6, 0.3, and 0.1 for the DCI, average signal shape, and decay time DOI estimates, respectively. The weighted average DOI estimate resulted in a 5%–8% improvement in DOI positioning error compared to DCI estimation alone for each crystal.

3.A.2. Light collection and energy resolution

Using the two sides stepped coating configuration, depth-dependent changes in energy spectra were investigated [Fig. 9(a)]. For irradiation depths near the phosphor-coated region, the photopeak is shifted to lower energies due to the low PMT quantum efficiency at 530 nm and greater light loss through the phosphor coating. Changes in light collection (photopeak position) for all coating configurations are given in Fig. 9(b). Consistent with energy spectra, all coated crystals show a monotonic decrease in light collection as the irradiation depth increases toward the top of the crystal.

To counteract depth-dependency of light collection and recover satisfactory energy resolution with head-on irradiation, the correlation between a depth metric and light collection was investigated. Using the two sides stepped coating configuration, the correlation of energy and DCI for each energy-valid event is demonstrated along with the trend of photopeak position vs DCI (red line) derived from side-on data.

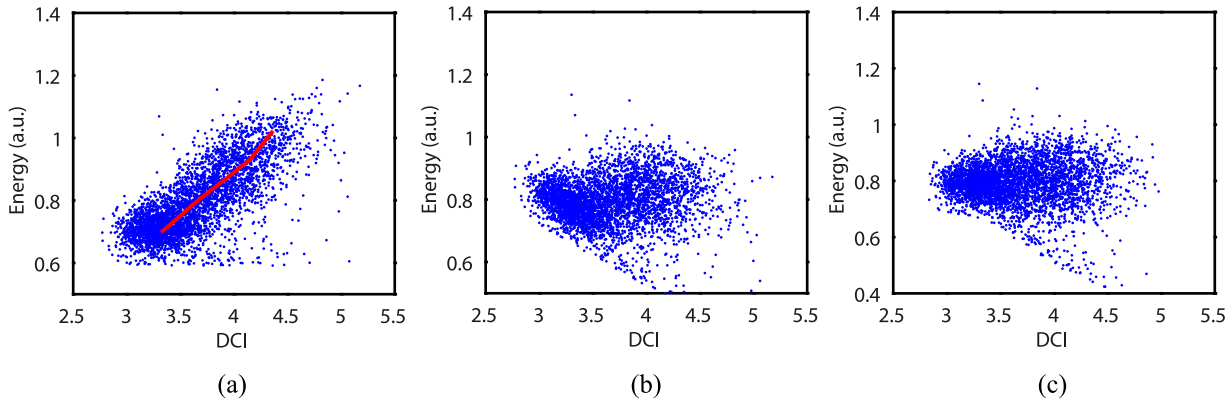

FIG. 10. (a) Correlation of light collection with DCI. The expected correlation based on side-on trends for photopeak position vs DOI and mean DCI vs DOI is given by the red line. (b) Corrected energy data based on the side-on correlation of energy and DCI. (c) Corrected energy using the nonlinear correlation method. Only a subset of the data is shown for clarity.

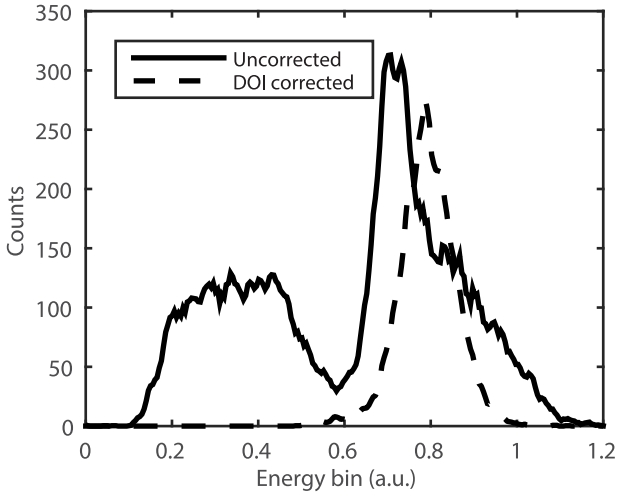

FIG. 11. Uncorrected energy spectra (solid) and DOI corrected photopeak (dashed) using the DCI-based energy depth dispersion correction.

Clearly, the side-on trend does not sufficiently describe the measured head-on correlation and does not optimally correct the depth-dependency of light collection when used as a measure of correlation [Fig. 10(b)]. Therefore, a nonlinear correction algorithm was developed to counteract depth-dependency of light collection. Energy data within the energy window were grouped into 10 bins according to their DCI value and the mean energy was calculated for the events in each DCI bin. All energy data in each bin were offset according to the difference between the bin's mean energy and the overall mean energy of all photopeak events [Fig. 10(c)]. In this way, the mean energy of photopeak events was consistent before and after applying the correction to avoid artificially improving energy resolution. Various numbers of DCI bins were investigated (5–35) to group energy data; however, the energy correction results were largely independent of the number of bins for this range. This is likely because the blurring of energy data was dominated by the DOI resolution when at least 5 DCI bins are used.

TABLE I. Single crystal energy resolution for fixed-depth irradiation and head-on with DOI correction.

	Head-on corrected (%)	Average side-on (%)
Uncoated	13.6 ± 0.1	13.1 ± 0.6
Top	14.7 ± 0.2	13.5 ± 1.2
One side	15.2 ± 0.2	13.7 ± 0.9
One side + top	15.9 ± 0.2	13.8 ± 0.8
Two sides stepped	16.7 ± 0.2	14.8 ± 1.0
Two sides	16.8 ± 0.3	14.8 ± 1.5

The depth-corrected photopeak for the two sides stepped coating configuration is shown in Fig. 11. As demonstrated in the energy spectrum, the nonlinear depth correction recovers the Gaussian nature of the photopeak. The Compton scattered events are not present in the DOI corrected spectrum since the correction was only applied to events within the 420–750 keV energy window (applied to raw energy values). Table I summarizes average fixed-depth and depth-corrected head-on energy resolutions for all coating configurations. The nonlinear energy correction method nearly recovers the average side-on energy resolution for all coated crystals and the discrepancy between the mean side-on and depth corrected values is less than 2% for all coating configurations. The head-on uncoated energy resolution was 13.6% while the head-on depth-corrected energy resolutions of the coated crystals were <17%.

3.A.3. Timing resolution

Estimated coincidence timing resolution vs DOI was computed for each coating configuration [Fig. 12(a)]. Timing resolution is degraded at depths corresponding to phosphor-coated regions due to the PMT's lower detection efficiency at 530 nm

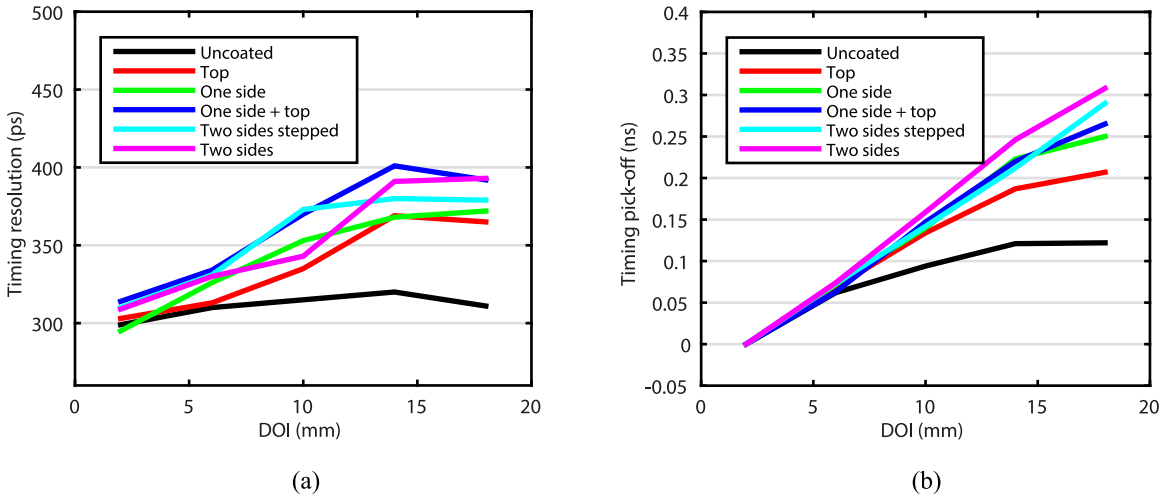

(a) (b)

FIG. 12. (a) Timing resolution obtained with side-on irradiation for all coating configurations. All crystals showed similar timing resolution at 2 mm (closest to PMT face) due to minimal absorption of scintillation light by the phosphor coating. (b) Trends of timing pick-offs (mean time in timing spectra) vs DOI. All values are offset to the respective value at 2 mm. Coated crystals show a larger end-to-end difference in timing pick-offs due to strong dependence of light collection on DOI.

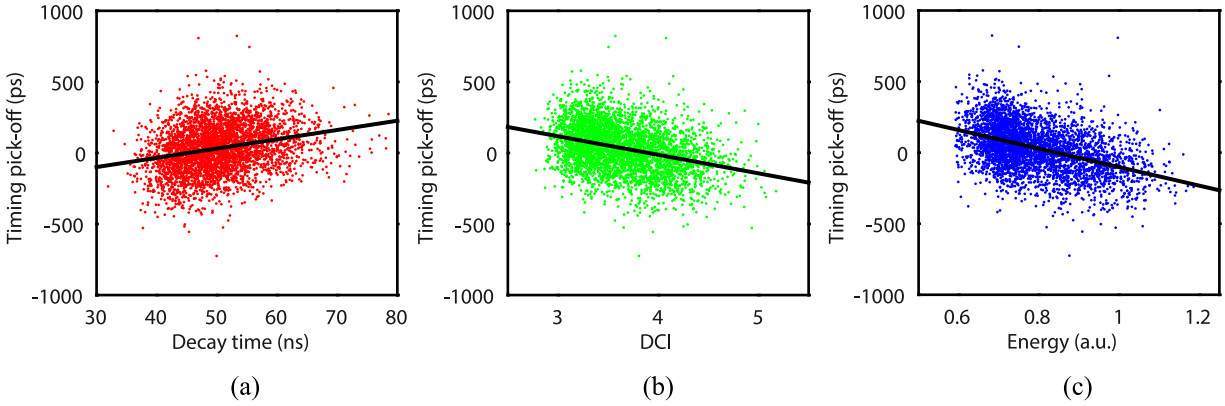

FIG. 13. Correlation of leading edge timing pick-offs with (a) decay time, (b) DCI, and (c) energy using the two sides stepped coating configuration. Only a subset of the data is shown for clarity.

and the delayed emission of YAG:Ce converted light. When a photon is absorbed by the phosphor, it is emitted according to the decay time of YAG:Ce (58 ns) which renders the photon less effective for timing purposes since timing resolution depends on the photoelectrons produced in the first nanoseconds of the pulse. We further investigated depth dispersion of timing pick-offs for each coating configuration with leading edge discrimination [Fig. 12(b)]. To clearly demonstrate differences, timing pick-offs for each coating configuration were offset according to their value at 2 mm DOI position. Phosphor coating introduces large depth dispersion of timing pick-offs compared to the uncoated crystal.

Since depth dispersion of timing pick-offs (time-walk) will manifest as blurring in the head-on timing data, correlations between timing pick-off and decay time, DCI and energy metrics were investigated using head-on data (Fig. 13). Timing pick-off values show good correlation with DCI and energy values, while weaker correlation with decay time, consistent with DOI encoding results. Head-on timing data were corrected based on a linear fit for each correlation.

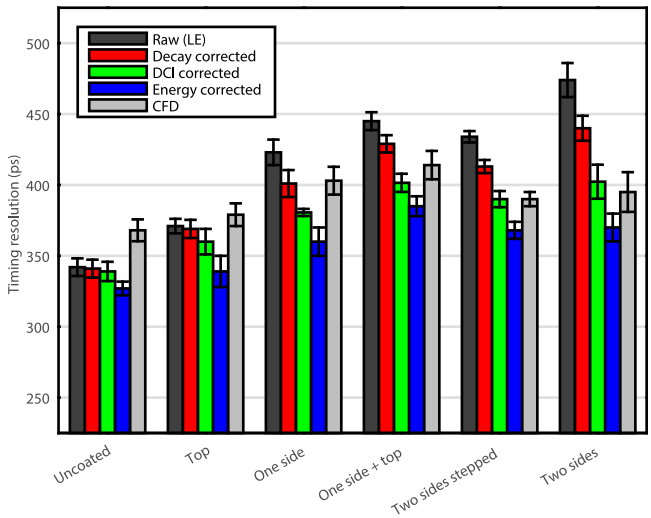

FIG. 14. Timing resolution for all coating configurations and depth-dispersion correction method. Energy-based correction provides the optimal timing resolution for all configurations.

Estimated coincidence timing resolution (using head-on data) was computed for each coating configuration and time-walk correction method (Fig. 14). Time-walk correction based on energy provides the best timing resolution while decay time based correction provides the poorest. The phosphor-coated crystals show slightly degraded timing resolution, from 10 to 50 ps, corresponding to 3%–15%, degradation from the uncoated crystal. Time pick-off correction based on energy correlation likely provides the best timing resolution for the following reason. Given that the energy values are correlated with DOI [Fig. 9(b)], correlation of timing pick-offs with energy provides a sufficient depth dispersion correction. Along with this, energy-based time walk correction also accounts for biases in timing pick-off that are not depth-dependent, such as those caused by the scintillator's intrinsic energy resolution leading to variations in the rising edge slope. We also applied a second order correction where the energy corrected timing pick-offs were then corrected according to their correlation with DCI values. However, there was no improvement in timing resolution with this second order correction compared to the energy-based time-walk correction.

3.B. Block detector module

The same analysis as described for the single crystals was applied to each crystal in the block detector. After characterizing the original uncoated detector module, the crystals in one 6×6 quadrant were removed from the light guide and recoupled to investigate any changes as a result of the removal and recoupling process. No changes in the flood histogram, energy, or timing resolution were observed. Sections 3.B.1–3.B.4 describe the results obtained for each coated quadrant compared to the original uncoated detector module. All results are summarized in Table II. The uncertainty in the values of Table II represent ±one standard deviation of the corresponding values considering all 36 crystals in a quadrant. The results from the single crystal experiments are given below the block detector values in parentheses. The one side + top coating configuration was not investigated with the block detector since it displayed the poorest timing resolution and moderate DOI positioning accuracy with single crystal experiments.

TABLE II. Summary of results obtained with the block detector module.

	Energy resolution (%)	Decay time (ns)	Timing resolution (ps)	DOI error (mm)	Resolvability index
Uncoated	13.8 ± 1.0 (13.6 ± 0.1)	42.2 ± 1.3 (42.5 ± 0.2)	404 ± 21 (327 ± 5)	n/a	0.44 ± 0.12
Top	16.6 ± 2.0 (14.7 ± 0.2)	53.0 ± 2.0 (47.2 ± 0.3)	461 ± 21 (339 ± 11)	5.2 ± 0.6 (3.9 ± 0.2)	0.52 ± 0.16
One side	20.4 ± 1.9 (15.2 ± 0.2)	52.8 ± 2.2 (49.0 ± 0.2)	442 ± 27 (360 ± 10)	3.6 ± 0.5 (2.3 ± 0.1)	0.54 ± 0.19
Two sides stepped	21.1 ± 2.3 (16.7 ± 0.2)	55.0 ± 1.6 (50.5 ± 0.3)	471 ± 22 (368 ± 6)	3.3 ± 0.3 (2.2 ± 0.1)	0.55 ± 0.18
Two sides	20.9 ± 2.9 (16.8 ± 0.3)	57.1 ± 1.5 (52.3 ± 0.1)	484 ± 25 (370 ± 10)	3.0 ± 0.3 (2.0 ± 0.1)	0.56 ± 0.20

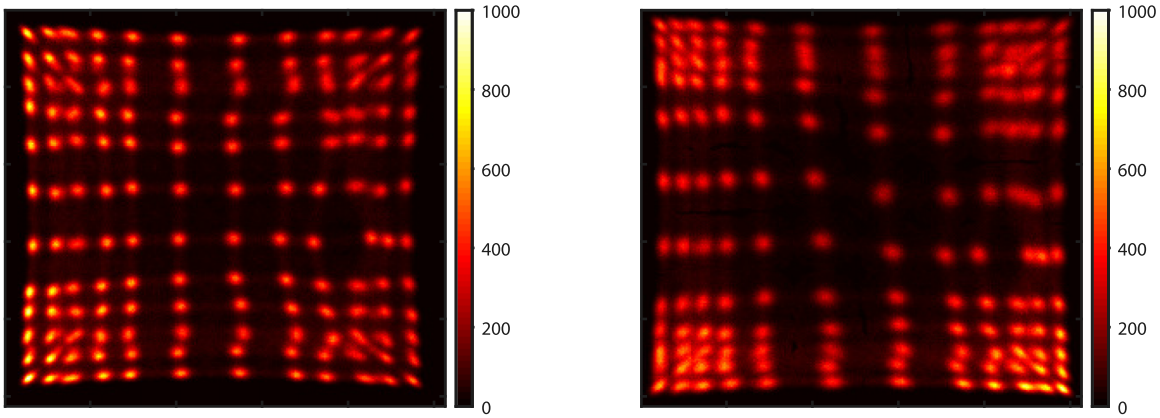

(a) (b)

FIG. 15. Flood maps obtained with (a) original uncoated module, (b) module after applying phosphor coatings to each quadrant. The orientation of the flood maps matches Fig. 3.

3.B.1. Flood maps

The flood maps obtained with the original uncoated block detector and after applying the phosphor coating to the crystals are shown in Fig. 15. All crystals can be clearly resolved with the original block detector and with the phosphor-coated module, with the exception of some crystals in the upper right quadrant (two sides coated).

Flood map quality was examined quantitatively using the following resolvability index (RI) metric:

$$\mathrm{RI}_j = \frac{\mathrm{FWHM}_j}{\frac{1}{n}\sum_{k\in n}|\mu_k - \mu_j|}. \quad (2)$$

For each jth crystal, vertical and horizontal intensity line profiles were obtained from the segmented flood maps and fitted with a Gaussian distribution. The average FWHM of the two Gaussian profiles is used as the numerator in Eq. (2). The mean from the Gaussian fit is used to determine the crystal's position in the flood histogram (μ). The average distance between the jth crystal and its n nearest neighbors is used to normalize the FWHM [denominator in Eq. (2)]. Depending on the crystal's location in the array, the number of nearest neighbors may be 4 (central 11×11 crystals), 3 (edges), or 2 (corners). From Table II, the crystal resolvability is degraded for the coated quadrants, with the top coating providing the best resolvability, and coating two sides the poorest. However, the resolvability values for all coated quadrants are ~0.5 meaning that on average, the distance between crystals is twice the FWHM of flood histogram spots, indicating satisfactory crystal decoding.

3.B.2. Energy resolution

Using the nonlinear, DCI-based energy correction, energy resolution was calculated for each crystal in the array. The average corrected head-on energy resolution and average energy resolution with side-on irradiation is summarized in Table III for each quadrant. Energy resolution in the block detector is in general poorer than with single crystals and is likely due to several factors: Single crystals showed superior DOI positioning accuracy because there is no optical crosstalk between crystals, which led to greater efficacy of the energy correction. The block detector readout including light sharing between PMTs causes some loss of scintillation light which will further degrade energy resolution compared to the ideal case of a single crystal directly coupled to a single PMT.

3.B.3. DOI encoding

Based on the single crystal results, only DCI-based pulse shape discrimination was used to estimate DOI with the block

TABLE III. Block detector average energy resolution for side-on irradiation and head-on with DOI correction.

	Head-on (%)	Side-on (%)
Uncoated	13.8 ± 1.0	13.5 ± 1.3
Top	16.6 ± 2.0	15.4 ± 1.4
One side	20.4 ± 1.9	16.3 ± 1.3
Two sides stepped	21.1 ± 2.3	17.5 ± 1.5
Two sides	20.9 ± 2.9	17.8 ± 1.9

detector. Similar DCI vs DOI trends were observed for each crystal in the array as measured with single crystals. DOI positioning errors were computed for each crystal in the array and the average DOI positioning error for each quadrant is summarized in Table II. Consistent with single crystal results, coating two sides of the crystals provided the smallest DOI positioning error while coating only the top surface provided negligible DOI information. In general, the DOI positioning error values obtained with the coated quadrants in the block detector are ~1 mm worse than those obtained with single crystals. This is likely due to several factors: the single crystals were individually wrapped with Teflon tape while ESR is used to separate crystals in the block detector. In many other studies, it has been shown that a diffuse reflector generally provides superior DOI resolution.[22,23] Second, mispositioned events will introduce greater DCI uncertainty as each crystal displays a unique DCI vs DOI relationship. Finally, beam broadening and intercrystal scatter with side-on measurements will introduce blurring of DOI metrics. For crystals in the central region of the array, the 511 keV photons must penetrate ~20 mm of LSO before interacting.

3.B.4. Timing resolution

A summary of average estimated coincidence timing resolutions for each quadrant obtained with all timing pick-off methods (leading edge or CFD/anode or dynode signals) is presented in Fig. 16. Based on single crystal results, only energy-based timing pick-off correction was used for leading edge discrimination and the correction was applied separately for each crystal. In all cases, leading edge discrimination with the dynode signal provides the best timing resolution. The original uncoated detector's timing resolution was 404 ps and coating one side showed the least degradation with a timing resolution of 442 ps (9% degradation). For all coating configurations, the best coincidence timing resolution was less than 500 ps. Average timing resolutions using leading edge discrimination with the dynode signal are summarized in Table II for each coating configuration.

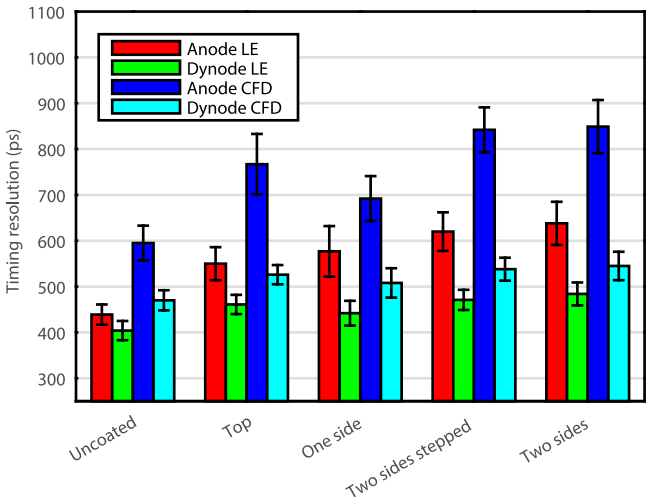

FIG. 16. Timing resolution for each coated quadrant using each timing pick-off method. Error bars represent ±one standard deviation of all crystals in the quadrant.

4. DISCUSSION

In our previous work, we demonstrated the potential of phosphor-coated crystals to provide combined TOF–DOI capabilities using short, single LSO crystals.[14,15] Here, we extended this work to long crystals and demonstrated the potential to translate phosphor-coated crystals for use in a clinical PET system by incorporating phosphor coating into a clinical block detector module, providing a simple and cost-effective solution to achieve TOF–DOI.

Although the energy resolution is somewhat degraded with the phosphor-coated crystals, it should be noted that the energy resolution of the original block detector was worse than what was reported for the mCT scanner (11.7%).[16] The detector used in this study was a prototype detector providing access to the common dynode signal and used an LSO crystal array optimized for timing resolution. It is likely that if phosphor coating is applied to crystals with better intrinsic energy resolution (~11%), head-on energy resolution of ~15%–16% may be possible. Along with this, different crystal surface treatments may lessen the depth-dependent light collection and provide better energy resolution.

Four phosphor-coating configurations were investigated simultaneously in a block detector module. All crystals were resolved in flood maps although the quantitative crystal resolvability with phosphor coated-crystals was slightly degraded compared to the original uncoated flood histogram. The flood map with phosphor-coated crystals shows the crystal spots are pulled toward the edges, decreasing the uniformity of the original (uncoated) flood map. It may be possible in future work to modify the light sharing design to counteract this with phosphor-coated crystals and recover some of the crystal resolvability performance.

Single crystal results showed DOI information could be achieved with a positioning error of ~2 mm and timing resolution was minimally affected (3%–15% degradation) compared to uncoated crystals. Timing resolution and depth encoding accuracy in the block detector were slightly degraded from single crystals, but still sufficient for TOF–DOI application. The best timing resolution with phosphor-coated crystals was 442 ps when only one side of the crystals was coated. This coating configuration provided a DOI positioning error of 3.6 mm, approximately a factor of two reduction from uncoated crystals and suitable for 2 or 3 bin DOI encoding. The best DOI positioning accuracy (3.0 mm) was obtained with crystals coated on two sides; however, this was achieved at a cost of degrading timing resolution to 484 ps.

The dynode signal consistently provided superior timing resolution with the block detector since the recorded dynode signal demonstrated improved noise properties compared to the anode sum signal. Whereas the dynode signals from all four PMTs are summed in the front-end electronics, the anode signals are summed in software, thus adding their respective electronic noise properties. It may be possible to achieve similar timing resolution using only the anode signals if an appropriate

preamplifier is implemented. However, it has been shown that the dynode signal provides superior timing resolution due to its faster initial rise-time, as the anode signal is compromised by a prompt inductive pickup.[24] In this work, the dynode signal provided a convenient method to extract timing and energy information without requiring summing and signal splitting amplifiers since the capacitive decoupled dynode signals were simply connected together on the voltage divider.

To allow flexibility in data analysis, a waveform digitizer was used to sample the PMT signals and pulse shape discrimination based on decay time, DCI, or average pulse shapes was performed using the fast sampling rate. However, the results presented are likely translatable to other electronics architectures. Specifically, DCI pulse shape discrimination only requires integrating the signal over two time periods, a task easily implemented with most electronics architectures found in modern clinical scanners.

These studies focused on a well-developed block detector module allowing all crystals to be easily resolved without requiring effort in developing a light guide or light sharing techniques. However, the specular reflector and light sharing used in this detector module may not be optimal for encoding depth-dependent signal shape changes with phosphor coating. In future work, we will construct a block detector using phosphor-coated crystals with optimized intercrystal reflector. We will also attempt to resolve smaller crystals and investigate alternative photodetectors, both position-sensitive photomultipliers and detectors with enhanced detection efficiency at longer wavelengths.

ACKNOWLEDGMENTS

This work was funded in part by a UC Davis Research Investment in Science and Engineering grant, by NIH Grant No. R01 CA170874 and a Natural Sciences and Engineering Research Council of Canada postgraduate fellowship (E.B.). The authors would like to thank the entire EXPLORER team for helpful discussions related to this work and Siemens Medical Solutions for providing the detector used in this study.

[a]Author to whom correspondence should be addressed. Electronic mail: eberg@ucdavis.edu

[1]J. K. Poon, M. L. Dahlbom, W. W. Moses, K. Balakrishnan, W. Wang, S. R. Cherry, and R. D. Badawi, "Optimal whole-body PET scanner configurations for different volumes of LSO scintillator: A simulation study," Phys. Med. Biol. **57**, 4077–4094 (2012).

[2]J. K. Poon, M. L. Dahlbom, J. Qi, S. R. Cherry, and R. D. Badawi, "Validation of SimSET Monte Carlo simulations of the Siemens Biograph mCT PET scanner," in *IEEE Nuclear Science Symposium Conference Record* (IEEE, 2012), pp. 2681–2684.

[3]X. Zhang, J. Zhou, G. Wang, J. K. Poon, S. R. Cherry, R. D. Badawi, and J. Qi, "Feasibility study of micro-dose total-body dynamic PET imaging using the EXPLORER scanner," Society of Nuclear Medicine and Molecular Imaging Annual Meeting, 2014.

[4]C. Tsigos and G. P. Chrousos, "Hypothalamic-pituitary-adrenal axis, neuroendocrine factors and stress," J. Psychosom. Res. **53**, 865–871 (2002).

[5]P. M. Price, R. D. Badawi, S. R. Cherry, and T. Jones, "Ultra staging to unmask the prescribing of adjuvant therapy in cancer patients: The future opportunity to image micrometastases using total-body ^{18}F-FDG PET scanning," J. Nucl. Med. **55**, 696–697 (2014).

[6]J. S. Karp, S. Surti, M. E. Daube-Witherspoon, and G. Muehllehner, "The benefit of time-of-flight in PET imaging: Experimental and clinical results," J. Nucl. Med. **49**, 462–470 (2008).

[7]M. Conti, "State of the art and challenges of time-of-flight PET," Phys. Med. **25**, 1–11 (2009).

[8]H. Thoen, V. Keereman, P. Mollet, R. Van Holen, and S. Vandenberghe, "Influence of detector parameters on lesion detectability for PET scanners with long axial FOV," Society of Nuclear Medicine and Molecular Imaging Annual Meeting, 2014.

[9]M. E. Casey and R. A. Nutt, "A multicrystal two dimensional BGO detector system for positron emission tomography," IEEE Trans. Nucl. Sci. **33**, 460–463 (1986).

[10]M. Ito, S. Hong, and J. S. Lee, "Positron emission tomography (PET) detectors with depth-of-interaction (DOI) capability," Biomed. Eng. Lett. **1**, 70–81 (2011).

[11]M. Schmand, L. Eriksson, M. E. Casey, M. S. Andreaco, C. Melcher, K. Wienhard, G. Flugge, and R. Nutt, "Performance results of a new DOI detector block for a high resolution PET—LSO research tomograph HRRT," IEEE Trans. Nucl. Sci. **45**, 3000–3006 (1998).

[12]E. Roncali, J. E. Phipps, L. Marcu, and S. R. Cherry, "Pulse shape discrimination and classification methods for continuous depth of interaction encoding PET detectors," Phys. Med. Biol. **57**, 6571–6585 (2012).

[13]H. Du, Y. Yang, J. Glodo, Y. Wu, K. Shah, and S. R. Cherry, "Continuous depth-of-interaction encoding using phosphor-coated scintillators," Phys. Med. Biol. **54**, 1757–1771 (2008).

[14]E. Roncali, J. P. Schmall, V. Viswanath, E. Berg, and S. R. Cherry, "Predicting the timing properties of phosphor-coated scintillators using Monte Carlo light transport simulation," Phys. Med. Biol. **59**, 2023–2029 (2014).

[15]J. P. Schmall, E. Roncali, E. Berg, V. Viswanath, J. Du, and S. R. Cherry, "Timing properties of phosphor-coated polished LSO crystals," Phys. Med. Biol. **59**, N139–N151 (2014).

[16]B. W. Jakoby, Y. Bercier, M. Conti, M. E. Casey, B. Bendriem, and D. W. Townsend, "Physical and clinical performance of the mCT time-of-flight PET/CT scanner," Phys. Med. Biol. **56**, 2375–2389 (2011).

[17]C. L. Melcher and J. S. Schweitzer, "Cerium-doped lutetium oxyorthosilicate: A fast, efficient new scintillator," IEEE Trans. Nucl. Sci. **39**, 502–505 (1992).

[18]E. Roncali, V. Viswanath, and S. R. Cherry, "Design considerations for DOI-encoding PET detectors using phosphor-coated crystals," IEEE Trans. Nucl. Sci. **61**, 67–73 (2014).

[19]E. Berg, E. Roncali, V. Viswanath, and S. R. Cherry, "Analysis of phosphor-coated crystal arrays: Towards a block detector for TOF-DOI PET," *IEEE Nuclear Science Symposium and Medical Imaging Conference, 2014*.

[20]Y. Yang, P. A. Dokhale, R. W. Silverman, K. S. Shah, M. A. McClish, R. Farrell, G. Entine, and S. R. Cherry, "Depth of interaction resolution measurements for a high resolution PET detector using position sensitive avalanche photodiodes," Phys. Med. Biol. **51**, 2131–2142 (2006).

[21]H. Anger, "Scintillation camera," Rev. Sci. Instrum. **29**, 27–33 (1958).

[22]K. C. Burr, A. Ivan, D. E. Castleburry, J. W. LeBlanc, K. S. Shah, and R. Farrell, "Evaluation of a prototype small-animal PET detector with depth-of-interaction encoding," IEEE Trans. Nucl. Sci. **51**, 1791–1798 (2004).

[23]Y. F. Yang, S. St. James, Y. Wu, H. Du, J. Qi, R. Farrell, P. Dokhale, K. S. Shah, K. Vaigneur, and S. R. Cherry, "Tapered LSO arrays for small animal PET," Phys. Med. Biol. **56**, 139–153 (2011).

[24]B. Bengston and M. Moszynski, "Timing improved by the use of dynode signals studied with different scintillators and photomultipliers," Nucl. Instrum. Methods Phys. Res. **204**, 129–140 (1982).